



THE UNIVERSITY *of* EDINBURGH

Edinburgh Research Explorer

Plate tephra; preserved bubble walls from large slug bursts during violent Strombolian eruptions.

Citation for published version:

Ruth, D & Calder, E 2014, 'Plate tephra; preserved bubble walls from large slug bursts during violent Strombolian eruptions.' *Geology*, vol. 42, no. 1, pp. 11-44. DOI: 10.1130/G34859.1

Digital Object Identifier (DOI):

[10.1130/G34859.1](https://doi.org/10.1130/G34859.1)

Link:

[Link to publication record in Edinburgh Research Explorer](#)

Document Version:

Peer reviewed version

Published In:

Geology

Publisher Rights Statement:

© 2013 Geological Society of America.

General rights

Copyright for the publications made accessible via the Edinburgh Research Explorer is retained by the author(s) and / or other copyright owners and it is a condition of accessing these publications that users recognise and abide by the legal requirements associated with these rights.

Take down policy

The University of Edinburgh has made every reasonable effort to ensure that Edinburgh Research Explorer content complies with UK legislation. If you believe that the public display of this file breaches copyright please contact openaccess@ed.ac.uk providing details, and we will remove access to the work immediately and investigate your claim.



1 Plate tephra: Preserved bubble walls from large slug bursts
2 during violent Strombolian eruptions

3 Dawn C.S. Ruth^{1*} and Eliza S. Calder^{1,2}

4 ¹*Department of Geology, 411 Cooke Hall, Buffalo, New York 14260, USA*

5 ²*School of Geosciences, Grant Institute, The King's Buildings, West Mains Road,*
6 *University of Edinburgh, Edinburgh EH9 3JW, UK*

7 *E-mail: dcs34@buffalo.edu.

8 **ABSTRACT**

9 Unusual “plate tephra” are described and provide key information about rarely
10 observed processes occurring during volcanic eruptions. The tephra formed during the
11 2008–2009 eruption of Llaima volcano, Chile and dispersed as far as 9 km from the vent.
12 The plates are angular clasts of vesicular basaltic-andesite ranging in size from 1 to 14
13 cm and in thickness from 2 to 5 mm. External features such as ridges, varying degrees of
14 curvature, and adhered material are present. Internal textures include strong crystal
15 alignment and deformed enclaves. We propose that the plates are wall fragments formed
16 during the rupture of large gas slugs associated with unsteady fire fountaining during the
17 violent Strombolian phase of the eruption. The presence of plate tephra may be a
18 diagnostic feature of highly unsteady activity where slug rupture is concurrent with the
19 formation of a sustained eruption column.

20 **INTRODUCTION**

21 Distinct vesicular, basaltic andesite plates produced during the violent
22 Strombolian opening phase of the 2008–2009 eruption of Llaima volcano, Chile, are

23 investigated. These clasts are part of the juvenile tephra that also included a bimodal
24 scoria population, characterized by brown and black scoria of low and high density,
25 respectively. The plates share morphological characteristics with other unusual tephra
26 such as pajaritos (Foshag and González, 1956), lava flakes (Maleyev and Vande-Kirkov,
27 1983), and limu o Pele (Schipper and White, 2010). Here we characterize the Llaima
28 plate tephra, investigate their origin, and present a formation model that explains their
29 morphological, textural, and dispersal characteristics. These plates represent an
30 overlooked fragmentation product in the context of violent Strombolian eruptions, yet
31 their generation has important implications for both conduit and plume processes.

32 **2008–2009 ERUPTION OF LLAIMA**

33 Llaima is a basaltic andesite stratovolcano (3125 m a.s.l. [above sea level])
34 located in the Southern Volcanic Zone of the Chilean Andes (Fig. 1), which erupted on
35 average every 5–6 yr over the past 400 yr (Dzierma and Wehrmann, 2010). The latest
36 eruption began on 1 January 2008 with violent Strombolian activity producing a
37 sustained eruption column 3.5–11 km in height. A tephra blanket was deposited to the
38 east-southeast, with thicknesses up to 11 cm (Smithsonian Institution, 2013a). The
39 opening phase lasted 13.5 h, and lower level activity continued occasionally until 21
40 February 2008. Periodic low-level Strombolian activity persisted until July 2008 and
41 waned by the end of April 2009 (Smithsonian Institution, 2013b).

42 **DEPOSIT DESCRIPTION**

43 Isopleth and isopach maps were produced for the tephra deposit (Fig. 2). For both
44 scoria, the isopleth dispersal axis is due east of the vent, whereas the plate isopleths mark
45 a more constrained zone to the east-southeast of the vent. Plate dimensions range from

46 major axis diameters of ~14 cm (6 km from the vent) to 1 cm (9 km from the vent). Over
47 the same area, black scoria range in size from 8 to 5 cm and the brown scoria from 7 to 3
48 cm (see the GSA Data Repository¹). Plate abundance is estimated at <1% of the deposit
49 by volume. It was not possible to distinguish whether they occupied a specific
50 stratigraphic position.

51 The average plate density is 813 kg m^{-3} , whereas black and brown scoria densities
52 are 583 kg m^{-3} , and 340 kg m^{-3} , respectively (Fig. 2a-c, insets). Eruption parameters were
53 calculated as follows: the deposit volume is $\sim 1.31 \times 10^6 \text{ m}^3$ after Bonadonna and Costa
54 (2012); and assuming a deposit density of 583 kg m^{-3} , the mass eruption rate (MER) for
55 the opening 13 h, 36 min, is $\sim 1.6 \times 10^4 \text{ kg s}^{-1}$ after Pioli et al. (2008).

56 **TEPHRA CHARACTERISTICS**

57 **Hand Sample Textures**

58 Plate shapes are oblate to bladed based on the Zingg shape parameter (Zingg,
59 1935; Wilson and Huang, 1979) (Fig. 3a) (Table 1). Minor axis dimensions are relatively
60 constant (~4 mm), irrespective of plate size. By contrast, both scoria are generally equant
61 to prolate. Approximately 90% of the 120 plates collected show curvature (Figs. 3b and
62 3c), but ~5% are folded with the edges tacked together. Scoria fragments are found
63 adhered to either surface. Major-axis parallel ridges and tension cracks are present on the
64 plate surfaces, occasionally on both sides.

65 **Microscopic Textures**

66 Thin sections show contrasting vesicularity and crystallinity for the three clast
67 types (see the Data Repository, Fig. 4). Vesicularity in the black scoria is moderate to
68 high with a few large, convolute vesicles whereas the brown scoria has very high

69 vesicularity with abundant smaller, more homogeneous and rounded vesicles. In the
70 plates, vesicles are convolute (with roughness from impinging crystals) to rounded and
71 are well connected, often forming long trains of bubbles parallel to the major plane.

72 The black scoria are highly crystalline (~50%–60%; tachylite), whereas the brown
73 scoria has lower crystallinity (~10%–15%; sideromelane). Some brown scoria contain
74 clots of higher crystallinity magma which are similar to the black scoria. Crystallinity of
75 the plates ranges from 40 to 50 vol%, similar to that observed in the black scoria. The
76 black and brown scoria are texturally akin to the “high porphyricity” (HP) and “low
77 porphyricity” (LP) scoria at Stromboli, respectively (Francalanci et al., 2004).

78 In all tephra, the mineralogy is mostly plagioclase with minor olivine (Fig. 4a and
79 4b). Plagioclase phenocrysts are 10–15 vol% of the overall crystal population, are
80 euhedral to subhedral, sieve textured with growth rims, and occasionally occur as
81 glomerocrysts. Olivine represent ~1 vol% of the total crystal population are subhedral to
82 anhedral with visible melt inclusions. The groundmass for all tephra is mostly plagioclase
83 microlites. Minor amounts of pyroxene and Fe-Ti spinel (<10 µm) are present in the
84 black scoria and plates.

85 A striking internal textural feature unique to the plates is the ubiquitous alignment
86 of crystals (Fig. 4c). Plagioclase and olivine phenocrysts and plagioclase microlites are
87 parallel to subparallel to the plate-parallel plane. Relatively large, dark enclaves, with
88 high Fe-Ti spinel and pyroxene content, are also present (Figs. 4a and 4b). The enclaves
89 are aligned relative to the major plane and show pinch-and-swell features. Neighboring
90 crystals and spinel-rich bands bend around the enclaves and glomerocrysts where present.

91 **SIMILAR TEPHRA FROM ELSEWHERE**

92 Similar tephra have been found elsewhere including pajaritos from Parícutin,
93 Mexico (Foshag and González, 1956; Pioli et al., 2008) and lava flakes from Tolbachik,
94 Russia (Maleyev and Vande-Kirkov, 1983). Pajaritos are microvesicular sideromelane
95 plates, centimeteres in diameter that show partial folding, and have external millimeter
96 size ridges (Pioli et al., 2008). Lava flakes are 5–20 cm diameter, 1–3 mm thick, slightly
97 vesicular, and show deformation (Maleyev and Vande-Kirkov, 1983). Only Maleyev and
98 Vande-Kirkov (1983) proposed that the plates represented ruptured bubbles walls, but
99 both studies associated these clasts with violent, pulsating, Strombolian activity.

100 Small (millimeter size) glassy, non-vesicular plates, termed limu o Pele, are
101 observed at lava flow ocean entries and in submarine deposits, notably at Lo’ihi volcano,
102 Hawaii (Schipper and White, 2010). Again, formation models involve the inflation and
103 rupture of basalt bubbles produced by either trapped super-heated seawater (Clague et al.,
104 2000), and/or from magmatic gases associated with Strombolian eruptions (Clague et al.,
105 2003).

106 **CONCEPTUAL MODEL OF FORMATION**

107 We suggest that pajaritos, lava flakes, and the Llaima plates are formed by the
108 same mechanism and recommend the umbrella term “plate tephra” be used to describe
109 similar clasts in the future. Our model elaborates on the basic model invoked by Maleyev
110 and Vande-Kirkov (1983) and accounts for a number of common features of these clasts.

111 We interpret the distinct shape of the plates, as well as internal textures, as caused
112 by extensional thinning of a magma film originating as walls of large slugs (several to
113 tens of meters in diameter) (Fig. 5a). In this model, expanding bubbles, near or above the
114 vent, experience film thinning, ductile deformation, and then undergo a primary phase of

115 inertial fragmentation, generating large, possibly sheet-shaped tatters of magma. During
116 flight, these ductile tatters are subject to chaotic rotation, torsion, and tension, as well as
117 cooling. Upon cooling to the glass transition temperature and thinning to a critical film
118 thickness of ~4 mm, they fragment brittly forming the observed angular plates. The
119 plates, instead of being ejected ballistically, were entrained into the eruption column and
120 dispersed according to their interaction with the wind field.

121 Strong crystal alignment during bubble expansion has been reproduced
122 experimentally (Yu et al., 2008). Furthermore, the near perfect crystal alignment with the
123 plate-parallel plane is typically formed in pure shear conditions associated with thinning
124 and extension (Manga, 1998). The observed pinch-and-swell enclaves and flow banding
125 are characteristics inherited at this stage. We infer that initial fragmentation of the bubble
126 film produces fluidal ejecta (on the basis of video observations), so primary
127 fragmentation is inertial, rather than brittle, in nature (Namiki and Manga, 2008).
128 Possible film retraction and additional plastic deformation of these plate parent particles
129 is evident in the form of the surface ridges (i.e., wrinkles, see Debrégeas et al., 1998),
130 variable curvature, tacked edges, and adhered material. The observed cracks are
131 interpreted as tension fracturing of a cooler, brittle crust covering ductile interior. Finally,
132 the abrupt selvages and lack of thinning at the edge of individual plates imply a
133 secondary brittle fragmentation event, probably occurring in the eruption column.

134 Online videos of the eruption show highly unsteady fire fountaining punctuated
135 by discrete slug bursts occurring tens to hundreds of meters above the vent (Fig. 5a).
136 Illustrative screen shots of footage from 23:00 on 1 January 2008–04:00 on 2 January
137 2008 (local time) (Figs. 5b and 5c) shows the continued advance and expansion of a

138 fragmentation front populated by large sheets and clots of lava from a recently ruptured
139 slug. In the video, fire fountaining resumes shortly after this particular slug rupture.

140 **IMPLICATIONS**

141 **Material Behavior**

142 The plate tephra experience significant rheological changes during the entire
143 formation process. Their complex deformation and fragmentation history is determined
144 by both cooling-related and strain-rate dependent behavior of magma. The limu o Pele
145 have distinctive features (see Schipper and White, 2010), which unlike those of the
146 subaerial plates, are determined by rapid quenching ($10^{5.31} \text{ K s}^{-1}$; Potuzak et al., 2008)
147 before fragmentation (i.e., quench granulation; Maicher et al., 2000; Schipper et al.,
148 2013). Calculated minimum quench rates for the Llaima plate tephra range from 2 to 5 K
149 s^{-1} (see the Data Repository), about six orders of magnitude slower than limu o Pele.
150 Thus, initial fragmentation occurs prior to the completion of cooling, allowing for post-
151 fragmentation melt relaxation, plastic deformation, and material adhesion during flight.
152 Assuming the estimated quench rate and an eruption temperature of 1050 °C, the glass
153 transition temperature (700 °C; Gregg and Zimbelman, 2000) could be reached in ~1–3
154 min, allowing for secondary brittle fragmentation to occur during flight.

155 **Conduit Flow**

156 Magma provenance is inferred from internal textures in the tephra. The high
157 crystallinity and density of the plates and black scoria suggests this magma may have
158 originated near the conduit walls (e.g., Cimarelli et al., 2010), and/or that vesicle collapse
159 occurred during film thinning. The high vesicularity and low crystallinity of the brown

160 scoria suggests a hotter, more volatile-rich magma, that ascended from depth up the
161 center of the conduit.

162 Video observations indicate highly unsteady eruptive behavior, with intensity and
163 gas decoupling varying on minute to second time scales. The fire fountaining and
164 resultant scoria represent relatively high intensity and either limited gas decoupling (for
165 foam fragmentation), or complete decoupling (if an annular flow regime is achieved).
166 The plates and large slugs indicate periods of relatively low intensity with significant gas
167 decoupling. Rapidly fluctuating behavior is possible due to nonlinear coupling and
168 decoupling of ascending phases (i.e., magma and gas) (Darteville and Valentine, 2007),
169 which may be enhanced by viscosity variations in the conduit. According to Pioli et al.
170 (2009), the estimated MER of 10^4 kg s^{-1} implies limited gas decoupling and the
171 development of a sustained column, which corresponds with plume observations
172 (Smithsonian Institution, 2013a). Since MER is an eruption-averaged value, finer scale
173 variations in conduit flow behavior are not captured. In this context plates can be a useful
174 diagnostic feature of highly unsteady violent Strombolian eruptions.

175 **Plume Conditions**

176 Based on their planar shape and similar densities to the scoria, we infer the plates
177 had a lower fall velocity, as a function of increased surface drag and chaotic fall behavior
178 (e.g., tumbling and fluttering) (Foshag and González, 1956; Wilson and Huang, 1979;
179 Andersen et al., 2005; Pioli et al., 2008). This would have allowed increased transport of
180 the plates, with respect to the scoria, which is reflected in the factor of 2.5 difference in
181 the clast diameters at the same distance (Figs. 2a-2c). Further, the cross-wind distribution
182 of plates in the deposit was evidently limited with respect to the scoria; this likely relates

183 to the complex interaction of the plates with the wind field, such as possibly the
184 decoupling from the plume at lower heights.

185 **CONCLUSIONS**

186 We characterize an uncommonly reported type of plate-shaped tephra produced
187 during a violent Strombolian eruption at Llaima volcano. From morphological, textural
188 and video observations we infer the plates are formed by thinning and extension of a
189 magma film, followed by inertial fragmentation as large gas slugs emanate from the
190 conduit and rupture above the vent. The primary fragmentation results in thin sheets that
191 continue to deform in flight, eventually cooling and undergoing secondary, brittle
192 fragmentation to form the observed plates. They are formed during highly unsteady flow
193 where the bursting of discrete gas slugs punctuates the more sustained fire fountaining.
194 The plates are entrained into the eruption column, yet their distinct aerodynamic
195 properties result in slightly modified dispersal features with respect to the scoria. Finally,
196 this class of tephra although not common, is also not unique, and has been briefly
197 described previously under a variety of nomenclature. We propose that these should
198 collectively be termed plate tephra and suggest that they are an important diagnostic
199 feature of the highly unsteady flow conditions common in some violent Strombolian
200 eruptions.

201 **ACKNOWLEDGMENTS**

202 Funding provided by a Geological Society of America Graduate Student
203 Research Grant to Ruth and National Science Foundation grant EAR-0828070 to
204 Calder. Thanks to J. Cortés, D. Schonwalder-Angel, R. Leach, P. Whelley, and A.
205 Brownell for help in the field. Thanks to J. Ball, A. Graettinger, and G. Valentine for

206 helpful discussions. Useful comments were provided by C.I. Schipper and three
207 anonymous reviewers.

208 **REFERENCES CITED**

- 209 Andersen, A., Pesavento, U., and Wang, Z.J., 2005, Unsteady aerodynamics of fluttering
210 and tumbling plates: *Journal of Fluid Mechanics*, v. 541, p. 65–90,
211 doi:10.1017/S002211200500594X.
- 212 Bonadonna, C., and Costa, A., 2012, Estimating the volume of tephra deposits: A new
213 simple strategy: *Geology*, v. 40, p. 415–418, doi:10.1130/G32769.1.
- 214 Cimarelli, C., Di Traglia, F., and Taddeucci, J., 2010, Basaltic scoria textures from a
215 zoned conduit as precursors to violent Strombolian activity: *Geology*, v. 38, p. 439–
216 442, doi:10.1130/G30720.1.
- 217 Clague, D.A., Davis, A.S., Bischoff, J.L., Dixon, J.E., and Geyer, R., 2000, Lava bubble-
218 wall fragments formed by submarine hydrovolcanic explosions on Lo’ihi Seamount
219 and Kilauea Volcano: *Bulletin of Volcanology*, v. 61, p. 437–449,
220 doi:10.1007/PL00008910.
- 221 Clague, D.A., Batiza, R., Head, J.W., III, and Davis, A.S., 2003, Pyroclastic and
222 hydroclastic deposits on Loihi Seamount, Hawaii, *in* White, J.D.L., et al., eds.,
223 Explosive Subaqueous Volcanism: American Geophysical Union Monograph 140, p.
224 73–96.
- 225 Dartevelle, S., and Valentine, G.A., 2007, Transient multiphase processes during the
226 explosive eruption of basalt through a geothermal borehole (Námafjall, Iceland,
227 1977) and implications for natural volcanic flows: *Journal of Volcanology and*
228 *Geothermal Research*, v. 262, p. 363–384, doi:10.1016/j.epsl.2007.07.053.

- 229 Debrégeas, G., de Gennes, P.-G., and Brochard-Wyart, F., 1998, The life and death of
230 “bare” viscous bubbles: *Science*, v. 279, p. 1704–1707,
231 doi:10.1126/science.279.5357.1704.
- 232 Dzierma, Y., and Wehrmann, H., 2010, Eruption time series statistically examined:
233 probabilities of future eruptions at Villarrica and Llaima Volcanoes, Southern
234 Volcanic Zone, Chile: *Journal of Volcanology and Geothermal Research*, v. 193,
235 p. 82–92, doi:10.1016/j.jvolgeores.2010.03.009.
- 236 Foshag, W.F., and González, J., 1956, Birth and development of Parícutin Volcano
237 Mexico: *U.S. Geological Survey Bulletin*, v. 965, p. 355–489.
- 238 Francalanci, L., Tommasini, S., and Conticelli, S., 2004, The volcanic activity of
239 Stromboli in the 1906–1998 A.D. period: mineralogical, geochemical and isotope
240 data relevant to the understanding of the plumbing system: *Journal of Volcanology*
241 *and Geothermal Research*, v. 131, p. 179–211, doi:10.1016/S0377-0273(03)00362-7.
- 242 Gregg, T.K.P., and Zimbelman, J.R., 2000, Volcanic vestiges, *in* Zimbelman, J.R. and
243 Gregg, T.K.P., eds., *Environmental Effects on Volcanic Eruptions: From Deep*
244 *Oceans to Deep Space*: Amsterdam, Kluwer Academic and Plenum Publishers, p.
245 243–251.
- 246 Houghton, B.F., and Wilson, C.J.N., 1989, A vesicularity index for pyroclastic deposits:
247 *Bulletin of Volcanology*, v. 51, p. 451–462, doi:10.1007/BF01078811.
- 248 Maicher, D., White, J.D.L., and Batiza, R., 2000, Sheet hyaloclastite: density-current
249 deposits of quench and bubble-burst fragments from thin, glassy sheet lava flows,
250 Seamount Six, Eastern Pacific Ocean: *Marine Geology*, v. 171, p. 75–94,
251 doi:10.1016/S0025-3227(00)00109-2.

- 252 Maleyev, Y.F., and Vande-Kirkov, Y.V., 1983, Features of pyroclastics of the Northern
253 Breakthrough of the Great Tolbachik Fissure Eruption and the origin of its pale-grey
254 ash, *in* Fedotov, S.A. and Markhinin, Y.K., eds., The Great Tolbachik Fissure
255 Eruption: Geological and geophysical data 1975–1976: Cambridge, UK, Cambridge
256 University Press, p. 57–71.
- 257 Manga, M., 1998, Orientation distribution of microlites in obsidian: *Journal of*
258 *Volcanology and Geothermal Research*, v. 86, p. 107–115, doi:10.1016/S0377-
259 0273(98)00084-5.
- 260 Morgan, D.J., and Jerram, D.A., 2006, On estimating crystal shape for crystal size
261 distribution analysis: *Journal of Volcanology and Geothermal Research*, v. 154, p. 1–
262 7, doi:10.1016/j.jvolgeores.2005.09.016.
- 263 Namiki, A., and Manga, M., 2008, Transition between fragmentation and permeable
264 outgassing of low viscosity magmas: *Journal of Volcanology and Geothermal*
265 *Research*, v. 169, p. 48–60, doi:10.1016/j.jvolgeores.2007.07.020.
- 266 Pioli, L., Azzopardi, B.J., and Cashman, K.V., 2009, Controls on the explosivity of scoria
267 cone eruptions: Magma segregation at conduit junctions: *Journal of Volcanology and*
268 *Geothermal Research*, v. 186, p. 407–415, doi:10.1016/j.jvolgeores.2009.07.014.
- 269 Pioli, L., Erlund, E., Johnson, E., Cashman, K., Wallace, P., Rosi, M., and Delgado
270 Granados, H., 2008, Explosive dynamics of violent Strombolian eruptions: The
271 eruption of Parícutin Volcano 1943–1952 (Mexico): *Earth and Planetary Science*
272 *Letters*, v. 271, p. 359–368, doi:10.1016/j.epsl.2008.04.026.

- 273 Potuzak, M., Nichols, A.R.L., Dingwell, D.B., and Clague, D.A., 2008, Hyperquenched
274 volcanic glass from Loihi Seamount, Hawaii: *Earth and Planetary Science Letters*,
275 v. 270, p. 54–62, doi:10.1016/j.epsl.2008.03.018.
- 276 Schipper, C.I., Sonder, I., Schmid, A., White, J.D.L., Dürig, T., Zimanowski, B., and
277 Büttner, R., 2013, Vapour dynamics during magma-water interaction experiments:
278 hydromagmatic origins of submarine volcanoclastic particles (limu o Pele):
279 *Geophysical Journal International*, v. 192, p. 1109–1115, doi:10.1093/gji/ggs099.
- 280 Schipper, C.I., and White, J.D.L., 2010, No depth limit to hydrovolcanic limu o Pele:
281 analysis of limu from Lo’ihi Seamount, Hawai’i: *Bulletin of Volcanology*, v. 72,
282 p. 149–164, doi:10.1007/s00445-009-0315-5.
- 283 Institution, S., 2013a, Llaima: *Bulletin of the Global Volcanism Network*, v. 33,
284 [http://www.volcano.si.edu/world/volcano.cfm?vnum=1507-
285 11=&volpage=var#bgvn_3306](http://www.volcano.si.edu/world/volcano.cfm?vnum=1507-11=&volpage=var#bgvn_3306).
- 286 Institution, S., 2013b, Llaima: *Bulletin of the Global Volcanism Network*, v. 35,
287 [http://www.volcano.si.edu/world/volcano.cfm?vnum=1507-
288 11=&volpage=var#bgvn_3506](http://www.volcano.si.edu/world/volcano.cfm?vnum=1507-11=&volpage=var#bgvn_3506).
- 289 Wilson, L., and Huang, T.C., 1979, The influence of shape on the settling velocity of
290 volcanic ash particles: *Earth and Planetary Science Letters*, v. 44, p. 311–324,
291 doi:10.1016/0012-821X(79)90179-1.
- 292 Yu, G., Li, X., Lieber, C.M., and Cao, A., 2008, Nanomaterial-incorporated blown
293 bubble films for large-area aligned nanostructures: *Journal of Materials Chemistry*,
294 v. 18, p. 728–734, doi:10.1039/b713697h.
- 295 Zingg, T., 1935, *Beitrage zur Schotteranalyse [Ph.D. thesis]: Zurich, ETH, 141 p.*

296 **FIGURE CAPTIONS**

297 Figure 1. A: Location map of Llaima volcano, Chile. B: Southeast view of the eruption
298 plume (~3–5 km above the vent) produced on 15 January 2008. Courtesy of Juan Enrique
299 Llona.

300

301 Figure 2. Simplified isopleth maps for plate tephra (A), black (B), and brown (C) scoria.
302 Black dots denote sample locations. Average diameter (cm) was calculated from three
303 measured dimensions of the ten largest clasts at each location, where possible. For the
304 plates, the parenthetical values are the average diameter calculated from the major and
305 intermediate axes only, for easier comparison with scoria isopleths. The insets are the
306 density histograms for each tephra type. Density determined after Houghton and Wilson
307 (1989). D: Deposit isopach map with contours in centimeters.

308

309 Figure 3. A: Plot of axial ratios of plates and scoria, the tephra after Wilson and Huang
310 (1979). Note that the plates and scoria fall in separate fields. B: Assorted plates with
311 varied curvature and size. C: Image of curved plate tephra and the major-axis parallel
312 ridges.

313

314 Figure 4. A: Thin section image shown parallel to major axis of a plate exhibiting aligned
315 plagioclase and deformed enclaves. B: Backscattered electron (BSE) image of the
316 enclave in A. The plagioclases align around the enclave, which exhibits more Fe-Ti
317 spinel and pyroxene. Image obtained using a SU-70 Hitachi SEM at University at
318 Buffalo, New York, USA. C: Rose diagrams of the main mineral phases. Data plotted in

319 the northwest quadrant of the rose diagram were projected into the southeast quadrant to
 320 obtain the true average orientation. The horizontal axis is 0°. Axial ratios calculated using
 321 CSDSlice (Morgan and Jerram, 2006). Additional thin section images are shown in the
 322 Data Repository (see footnote 1).

323

324 Figure 5. A: Model for plate formation illustrating the relationship between conduit flow
 325 and resultant tephra type. B,C: Screen shots of the video at 1:33–1:35. Note, silhouette in
 326 the foreground right, corresponds to tree branches. B: Fragmentation front captured after
 327 a slug burst. C: Expanding fragmentation front of the same large ruptured slug as in B.
 328 Dashed lines in this image show the location of the fragmentation front in B.

329

330 ¹GSA Data Repository item 2013xxx, xxxxxxxx, is available online at
 331 www.geosociety.org/pubs/ft2013.htm, or on request from editing@geosociety.org or
 332 Documents Secretary, GSA, P.O. Box 9140, Boulder, CO 80301, USA.

333

334

335

TABLE 1. DIMENSION DATA FOR 2008–2009 TEPHRA

	n	Average Major Axis (cm)	Average Intermediate Axis (cm)	Average Minor Axis (cm)	Zingg (b/a) (intermediate/major)	Zingg (c/b) (minor/intermediate)
Plates	424	4.5 (±2.4)	3.3 (±1.8)	0.4 (±0.2)	0.7	0.1
Black scoria	1009	3.6 (±1.4)	2.5 (±1.2)	1.6 (±1.1)	0.7	0.6
Brown scoria	1025	2.9 (±1.3)	2.0 (±1.1)	1.3 (±0.8)	0.7	0.7

Note: Numbers in parentheses are 1σ standard deviation and n is number of clasts measured.

336

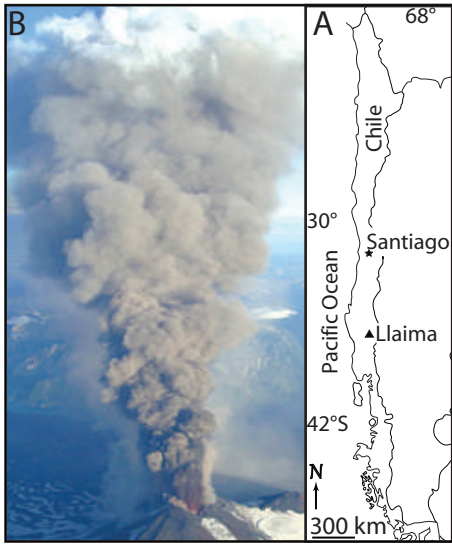


Figure 1

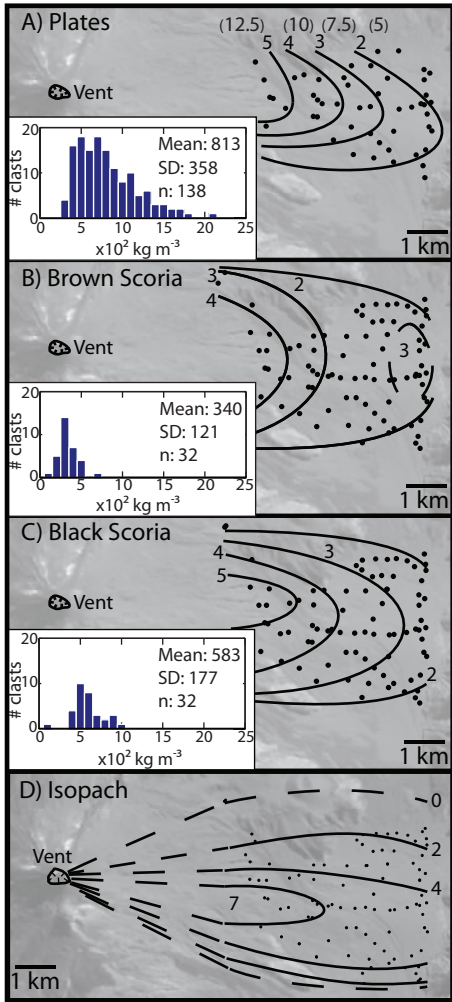
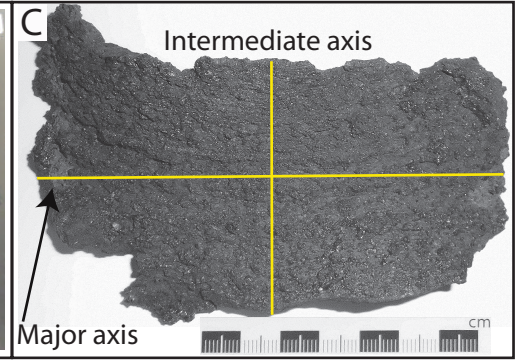
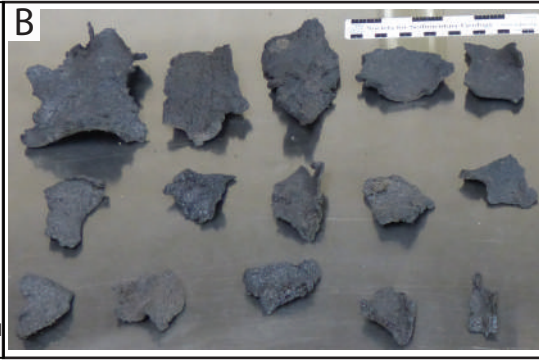
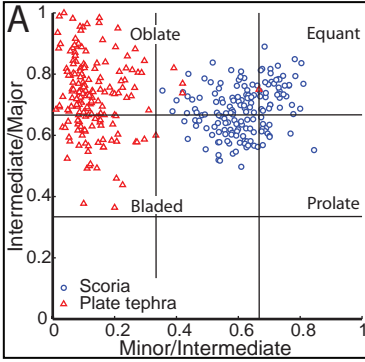


Figure 2



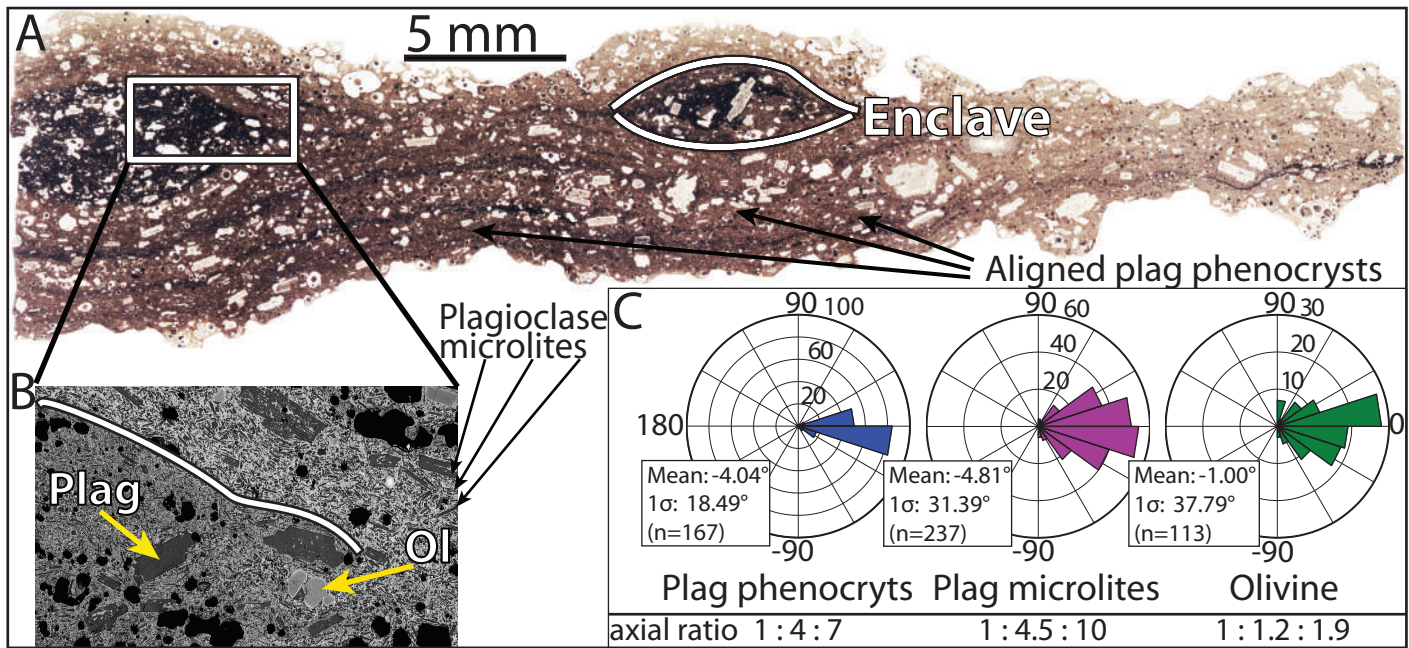


Figure 4

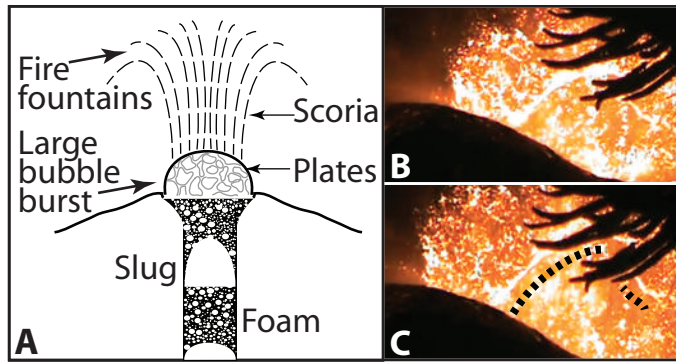


Figure 5

1 **SUPPLEMENTAL MATERIALS**

2 **Quench rate calculation**

3 Quench rates were estimated using the following equation (Xu and Zhang, 2002):

4
$$q=(T_{ae}-T_{ff})h/\rho C_p L$$

5 where T_{ae} is the apparent equilibrium temperature, T_{ff} is the glass transition temperature, h is the
6 heat transfer coefficient, ρ is material density, C_p is the heat capacity of basalt, and L is the
7 effective half thickness of the object (volume/surface area). We assumed an equilibrium
8 temperature of 1450 K, a glass transition temperature of 1000 K (Gregg and Zimbelman, 2000),
9 a heat transfer coefficient of $50 \text{ W m}^{-2} \text{ K}^{-1}$ (Robertson, 1988), a density of 2750 kg m^{-3} , and heat
10 capacity of $1200 \text{ J kg}^{-1} \text{ K}^{-1}$ (Greg and Zimbelman, 2000). To determine L , we assumed the plate
11 shapes were rectangular prisms with the dimensions reported in Table 1.

12 **Figures and Video**

13 Back scattered electron images of the brown and black scoria are provided for reference
14 (Fig. S1). Additional thin sections are provided to show the range of textures observed within the
15 plate tephra (Fig. S2).

16 Observations of one fragmenting slug concurrent with fire fountaining were conducted on
17 video provided by Patricio Oberg.

18 **References**

- 19 Gregg, T.K.P., and Zimbelman, J.R., 2000, Volcanic Vestiges, *in* Zimbelman, J.R. and Gregg,
20 T.K.P. eds., Environmental Effects on Volcanic Eruptions: From Deep Oceans to Deep
21 Space, Kluwer Academic/Plenum Publishers, p. 243-251.
- 22 Robertson, E.C., 1988, Thermal properties of rocks: U.S. Geologic Survey Open-File Report 88-
23 441, 106 p.
- 24 Xu, Z., and Zhang, Y., 2002, Quench rates in air, water, and liquid nitrogen, and inferences of
25 temperature in volcanic eruption columns: Earth and Planetary Science Letters, v. 200, p.
26 315-330.

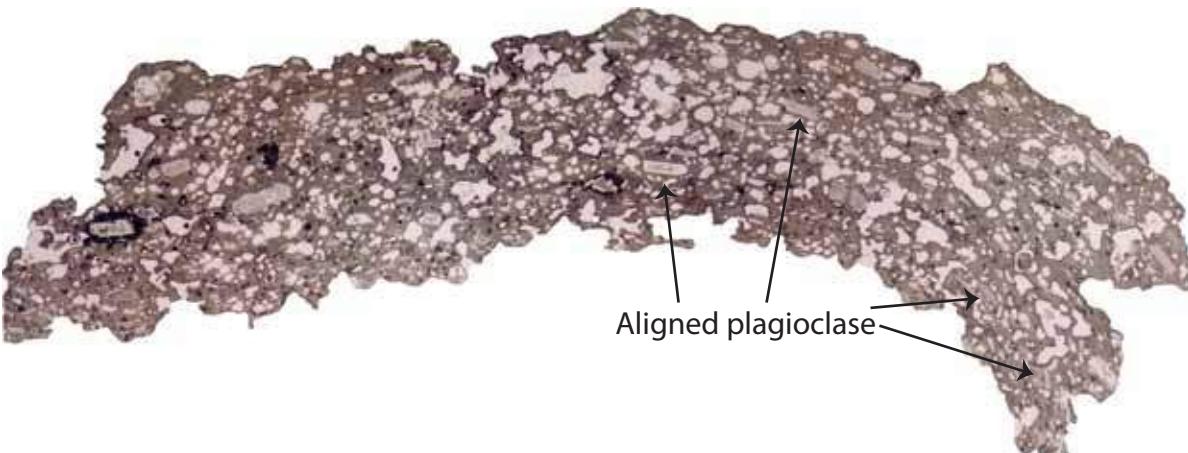
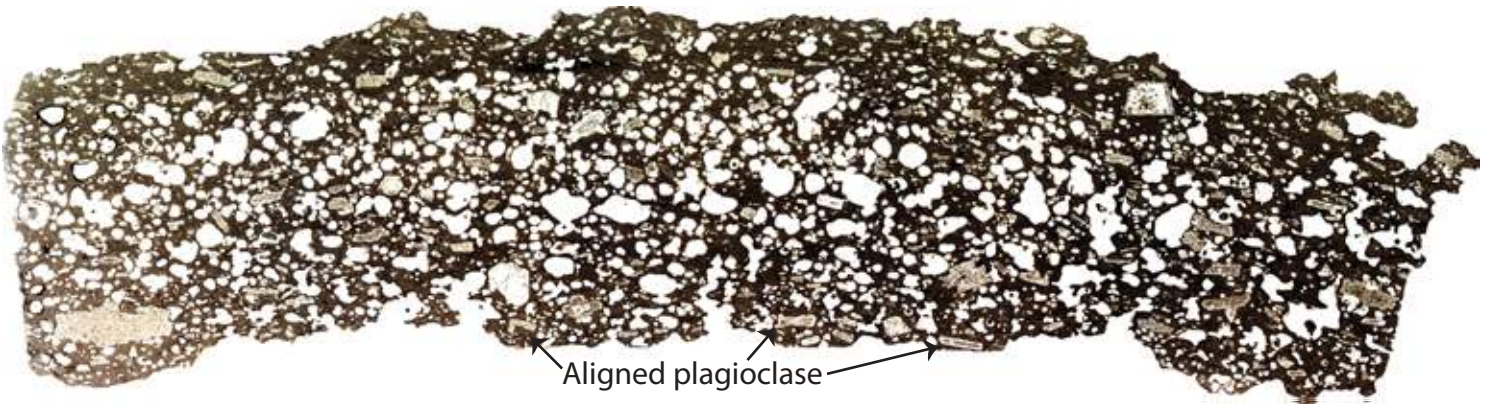
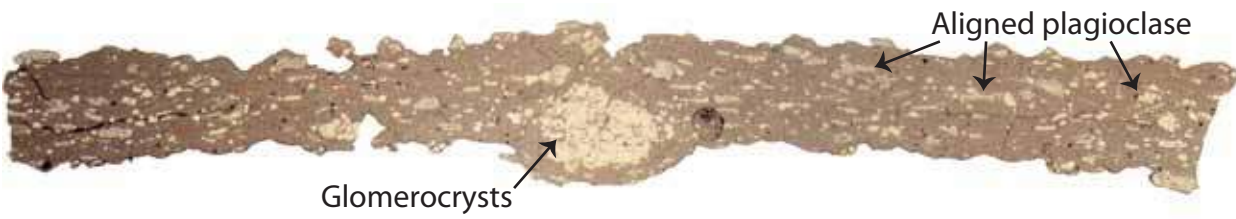
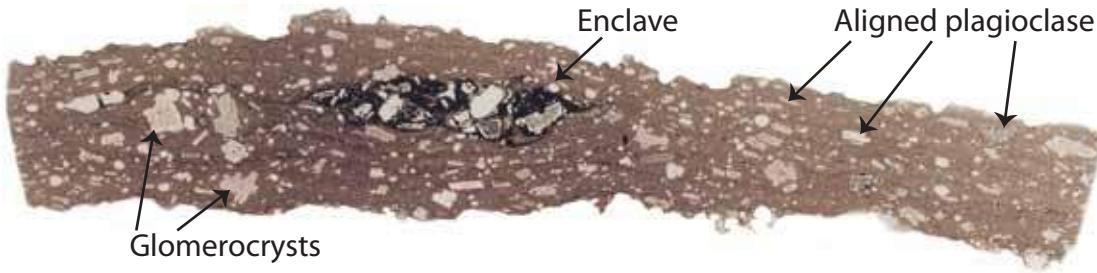
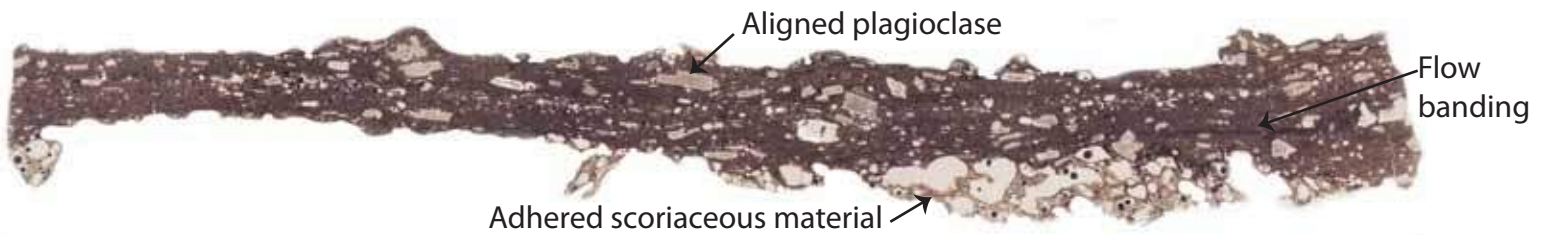
27 **FIGURE CAPTION**

28 Figure S1. Back-scattered electron images of brown scoria (A) and black scoria (B). Note that
29 images were collected at the same scale.

30 Figure S2. An assortment of plate tephra in thin section. All tephra are at approximately the
31 same scale. Note the ubiquitously aligned plagioclase crystals, the presence of flow banding and
32 wide range of vesicularity.

33

~3 cm



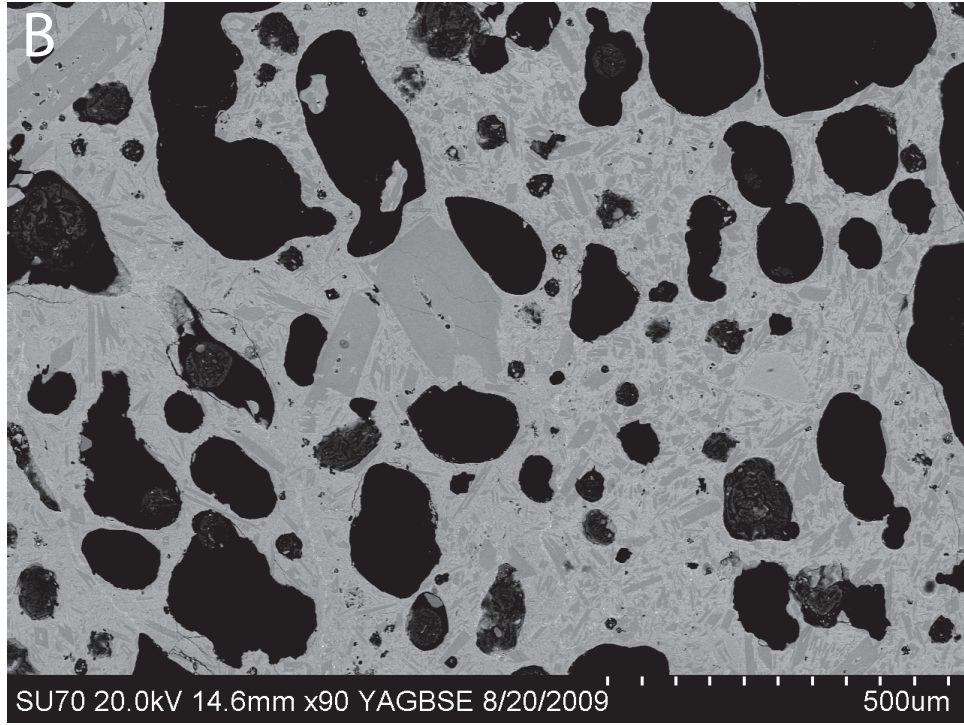
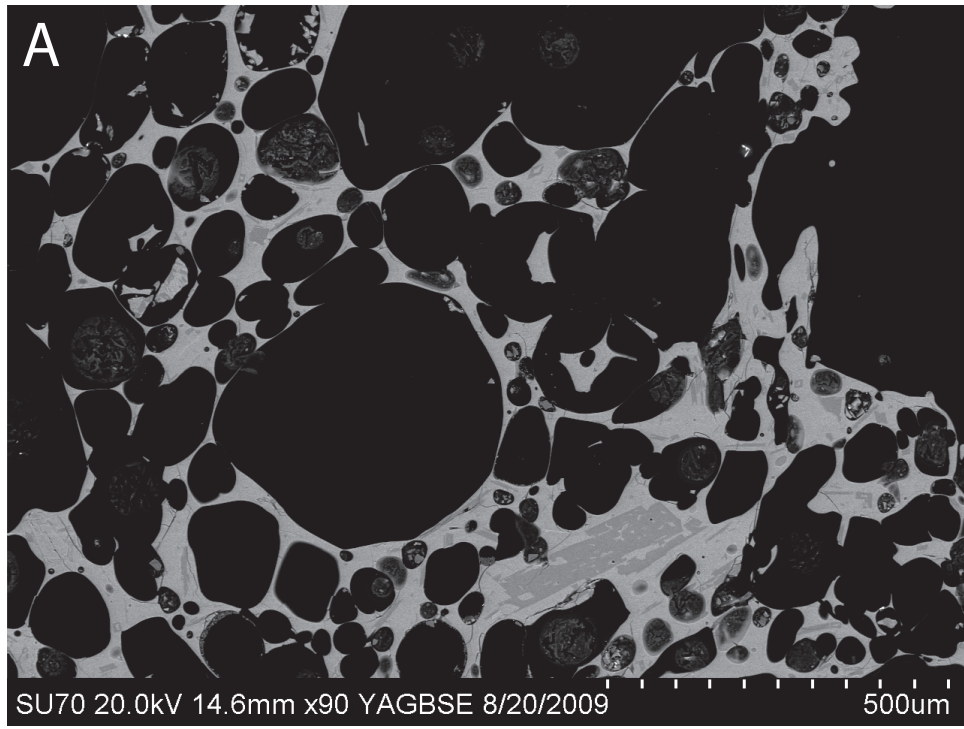


Figure S2